

Full Spectroscopic Model and Trihybrid Experimental-Perturbative-Variational Line List for ZrO

Armando N. Perri¹ , Fadia Taher^{2,3} , Laura K. McKemmish¹ *

¹*School of Chemistry, University of New South Wales, 2052, Sydney, Australia*

²*Faculty of Sciences II, Research Platform in Nanosciences and Nanotechnology, Laboratory of Experiments and Computation of Materials and Molecules (EC2M), Lebanese University, Campus Fanar, P.O. Box: 90656, Beirut, Lebanon*

³*Faculty of Engineering III, Laboratory of Molecular Quantum Mechanics and Modeling (MQMM), Lebanese University, Hadath Campus, Beirut, Lebanon*

9 August 2023

ABSTRACT

Zirconium monoxide (ZrO) absorption lines define rare S-type stars and are currently being sought on exoplanets. Successful detection is dependent on an accurate and comprehensive line list, with existing data not ideal for many applications. Specifically, the Plez *et al.* line list is near-complete but has insufficient accuracy for high-resolution cross-correlation, while the Sorensen & Bernath data has high accuracy but only considers a small number of spectral bands. This article presents a novel spectroscopic model, variational line list and trihybrid line list for the main ⁹⁰Zr¹⁶O isotopologue, as well as isotopologue-extrapolated hybrid line lists for the ⁹¹Zr¹⁶O, ⁹²Zr¹⁶O, ⁹³Zr¹⁶O, ⁹⁴Zr¹⁶O and ⁹⁶Zr¹⁶O isotopologues. These were constructed using Duo based on icMRCI-SD/CASSCF *ab initio* electronic data calculated using Molpro, experimental energies obtained from a previous MARVEL data compilation and perturbative energies from Sorensen & Bernath. The new ⁹⁰Zr¹⁶O ExoMol-style trihybrid line list, ZORRO, comprises 227,118 energies (13,075 experimental) and 47,662,773 transitions up to 30,000 cm⁻¹ (333 nm) between ten low-lying electronic states (X ¹Σ⁺, a ³Δ, A ¹Δ, b ³Π, B ¹Π, C ¹Σ⁺, d ³Φ, e ³Π, f ³Δ and F ¹Δ). The inclusion of experimental energy levels in ZORRO means ZrO will be much easier to detect using high-resolution ground-based telescopes in the 12,500 – 17,500 cm⁻¹ (571 – 800 nm) spectral region. The inclusion of variational energy levels means that the ZORRO line list has very high completeness and can accurately model molecular absorption cross-sections even at high temperatures. The ZORRO data will hopefully facilitate the first detection of ZrO in the atmosphere of a hot Jupiter exoplanet, or alternatively more conclusively exclude its presence.

Key words: molecular data, opacity, astrochemistry, astronomical data bases: miscellaneous, stars: chemically peculiar, planets and satellites: atmospheres

1 INTRODUCTION

Zirconium monoxide (ZrO) is a second-row transition metal diatomic molecule of astronomical significance. Notably, the strong absorption lines of ZrO are the characteristic spectral signature of rare S-type stars (Keenan 1954), which replace the prominent titanium monoxide (TiO) absorption lines of common M-type stars. It is known that S-type stars have an atmospheric carbon-to-oxygen ratio near unity and exhibit slow neutron-capture processes (s-processes) that lead to an overabundance of zirconium (Piccirillo 1980; Van Eck *et al.* 2017). ZrO is also faintly detectable in SC-type stars (Keenan & Boeshaar 1980), M-type stars (Bobrovnikoff 1934) and sunspots (Richardson 1931). There has been some search for ZrO in the atmospheres of hot Jupiter exoplanets without success (Tabernero *et al.* 2021; Borsa *et al.* 2021). All current

ZrO detections have been made using mid-resolution techniques from either space-based or ground-based telescopes. The former space-based telescopes are particularly useful for the detection of fainter objects, such as hot Jupiter exoplanets, and are promising in the new era of the James Webb Space Telescope (JWST). Despite this, high-resolution cross-correlation (HRCC) techniques using ground-based telescopes have become a critical technique over the last decade to detect new molecules in exoplanetary atmospheres (Brogi & Line 2018; Birkby 2018), where the Very Large Telescope (VLT) is often employed in combination with ultra-high precision spectrographs such as the most recent Echelle SPectrograph for Rocky Exoplanets and Stable Spectroscopic Observations (ESPRESSO) instrument. Cross-correlation is an effective method of signal filtration that facilitates the unambiguous astronomical detection of a molecule. This relies on high-resolution ground-based measurements that are compared to high-resolution model templates simulated from

* E-mail: l.mckemmish@unsw.edu.au

atomic and molecular line lists of sub cm^{-1} accuracy. High-resolution cross-correlation spectroscopy has been used to successfully identify many diatomic molecules, such as CO (Brogi & Line 2018), OH (Landman et al. 2021) and arguably TiO (Nugroho et al. 2017), in exoplanetary atmospheres. In order to achieve the required accuracy for such detections, it has been shown that experimentally-derived energies must be explicitly incorporated into a line list (McKemmish et al. 2019; Syme & McKemmish 2021). This is especially true for complex transition metal diatomic systems such as ZrO (Tennyson et al. 2016).

The current inability to detect ZrO in an exoplanetary atmospheres using high-resolution cross-correlation is not unexpected given the current state of line list data availability for ZrO. Specifically, for ZrO, the most complete line list available is from Plez (Plez et al. 2003; Van Eck et al. 2017), but this does not contain experimentally-derived energy levels and thus will not have the sub- cm^{-1} accuracy in the strong lines needed for this technique. The more accurate MoL-LIST line list (Bernath 2020; Sorensen & Bernath 2021) only considers the $B^1\Pi - X^1\Sigma^+$ rovibronic and $X^1\Sigma^+$ rovibrational transitions. This data thus misses many strong transitions, significantly increasing the required signal-to-noise for a molecular detection and greatly restricting the spectral range that can be used.

To enable effective use by astronomers with all modern techniques, a line list with both high accuracy for all strong lines positions and high completeness across temperature and spectral ranges is required. For ZrO, this is achieved using the approach outlined by Syme & McKemmish (2021) for the cyano radical (CN). Specifically, high accuracy is obtained with the high-resolution experimental MARVEL energies from McKemmish et al. (2018) complemented by a small number of interpolated perturbative (effective Hamiltonian) energies from Sorensen & Bernath (2021). High completeness can be created from a new spectroscopic model (fitted to experimental data) constructed herein that yields a variational line list. Finally, the experimental, perturbative and variational energies are combined to generate a novel trihybrid line list for $^{90}\text{Zr}^{16}\text{O}$, named ZORRO. Various isotopologue energies are predicted from this main line list using standard techniques, where ^{90}Zr , ^{91}Zr , ^{92}Zr , ^{93}Zr , ^{94}Zr and ^{96}Zr have an isotopic abundance of 51.5, 11.2, 17.1, 0.0, 17.4 and 2.8%, respectively (Nomura et al. 1983).

This article is structured as follows; an overview of the literature experimental, perturbative and *ab initio* spectroscopic data are presented in Section 2. The *ab initio* data calculated by Tabet et al. (2019) are also adapted. In Section 3, the spectroscopic model for the main $^{90}\text{Zr}^{16}\text{O}$ isotopologue is constructed. In Section 4, variational line lists are generated for the $^{90}\text{Zr}^{16}\text{O}$, $^{91}\text{Zr}^{16}\text{O}$, $^{92}\text{Zr}^{16}\text{O}$, $^{93}\text{Zr}^{16}\text{O}$, $^{94}\text{Zr}^{16}\text{O}$ and $^{96}\text{Zr}^{16}\text{O}$ isotopologues, as well as trihybrid and isotopologue-extrapolated hybrid line lists. In Section 5, various partition functions, lifetimes and cross sections of ZrO are analysed.

2 $^{90}\text{Zr}^{16}\text{O}$ SPECTROSCOPIC DATA

The rovibronic spectroscopy of ZrO is characterised by many low-lying electronic states as shown in Figure 1. This leads to a complex band structure with intense transitions arising from the singlet and triplet manifolds. From the Boltzmann

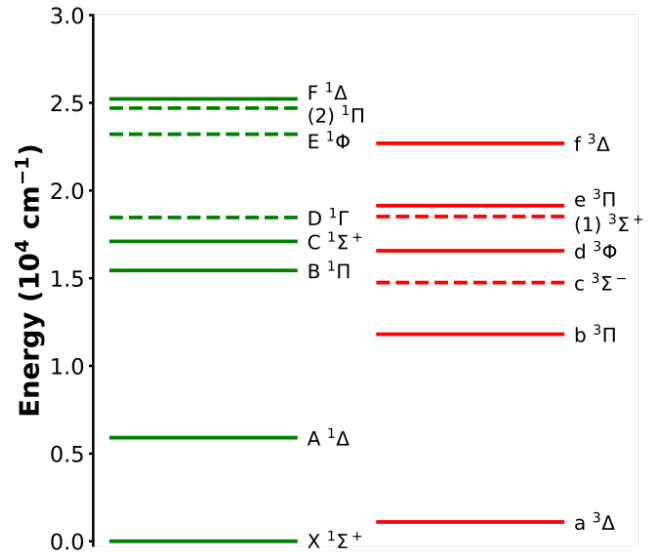


Figure 1. The electronic states of ZrO below $25,000 \text{ cm}^{-1}$ with term energies T_e from McKemmish et al. (2018) where available and from the MRCI calculations of Tabet et al. (2019) otherwise. The solid lines indicate electronic states considered in this work.

distribution, the $X^1\Sigma^+$ and $a^3\Delta$ electronic states have significant population such that the $B^1\Pi - X^1\Sigma^+$, α ($f^3\Delta - a^3\Delta$), β ($e^3\Pi - a^3\Delta$), γ ($d^3\Phi - a^3\Delta$) transitions dominate.

2.1 Experimental Data

In the literature, the main $^{90}\text{Zr}^{16}\text{O}$ isotopologue has been investigated through many experimental spectroscopic studies. This was recently reviewed and collated in McKemmish et al. (2018), which obtained assigned rovibronic transitions from twelve publications derived from both laboratory measurements and astronomical spectra. Using the MARVEL (Furtenbacher et al. 2007) algorithm, the 22,549 rovibronic transitions validated were inverted to give a set of empirical energies for rovibronic states belonging to the $X^1\Sigma^+$, $A^1\Delta$, $B^1\Pi$, $C^1\Sigma^+$, $F^1\Delta$, $a^3\Delta$, $b^3\Pi$, $d^3\Phi$, $e^3\Pi$ and $f^3\Delta$ electronic states. These energies form one self-consistent spectroscopic network containing 8,088 rovibronic states. Apart from unresolved Λ -doubling in several electronic states, all fine structure is characterised in accordance with Hund's coupling case (a).

2.2 Perturbative Line Lists

Beyond the experimental data collated by McKemmish et al. (2018), there exists only perturbative line lists for ZrO in the literature. The perturbative (or traditional) methodology relies on an effective Hamiltonian, where experimental data are fit to polynomial expressions through the optimisation of spectroscopic parameters for each electronic state. This approach allows for the prediction of unobserved transitions with *ab initio* dipole moment curves. This provides a natural extension to experimental data, where the associated line lists interpolate experimental energies to high accuracy. Due to corrections obtained through perturbation theory, however, perturbative line lists typically extrapolate poorly, especially

to higher vibrational levels. For this reason, they are often incomplete as they are limited by experimental data.

The most accurate ZrO perturbative spectroscopic line list in the literature was generated by [Sorensen & Bernath \(2021\)](#) for the $B^1\Pi - X^1\Sigma^+$ rovibronic and $X^1\Sigma^+$ rovibrational transitions. This perturbative analysis relied on a high temperature laboratory emission spectrum in combination with the *ab initio* $B^1\Pi - X^1\Sigma^+$ off-diagonal dipole moment curve calculated by [Langhoff & Bauschlicher \(1990\)](#). For reasonable completeness, however, astronomers are currently limited to the perturbative line list constructed by Plez ([Plez et al. 2003](#); [Van Eck et al. 2017](#)). This is the most comprehensive line list with transition intensities currently available for ZrO (superseded by this work), which was constructed in accordance with the TiO line list methodology of [Plez \(1998\)](#) using spectroscopic parameters from a range of sources. In particular, the Plez line list includes the $B^1\Pi - X^1\Sigma^+$, $C^1\Sigma^+ - X^1\Sigma^+$, $B^1\Pi - A^1\Delta$, $E^1\Phi - A^1\Delta$, $b^3\Pi - a^3\Delta$, $\gamma(d^3\Phi - a^3\Delta)$, $\beta(e^3\Pi - a^3\Delta)$ and $\alpha(f^3\Delta - a^3\Delta)$ rovibronic transitions for the $^{90}\text{Zr}^{16}\text{O}$, $^{91}\text{Zr}^{16}\text{O}$, $^{92}\text{Zr}^{16}\text{O}$, $^{93}\text{Zr}^{16}\text{O}$, $^{94}\text{Zr}^{16}\text{O}$ and $^{96}\text{Zr}^{16}\text{O}$ isotopologues.

There is no variational line list currently available for ZrO that has been constructed through numerical solution of the nuclear Schrödinger equation. This prevents reliable extrapolation to unobserved rovibrational states.

2.3 Ab Initio Data

Ab initio spectroscopic data have been calculated for many low-lying electronic states of ZrO. An important historical study was conducted by [Langhoff & Bauschlicher \(1990\)](#) for twelve electronic states using the MRCI/SA-CASSCF level of theory. Recently, an improved study was performed by [Tabet et al. \(2019\)](#) for twenty-four electronic states using a larger active space in the CASSCF calculations.

In this work, the *ab initio* study of [Tabet et al. \(2019\)](#) was adapted to consider larger bond lengths and explicitly calculate all off-diagonal dipole moment curves. These novel calculations were performed in Molpro 2020.1 ([Werner et al. 2020](#)) using the icMRCI-SD level of theory with reference orbitals obtained from SA-CASSCF calculations. Using the (a_1, b_1, b_2, a_2) irreducible representation of the C_{2v} point group, $(4, 2, 2, 1)$ active orbitals from (Zr: $4d, 5s, 5p$), $(2, 1, 1, 0)$ active orbitals from (O: $2s, 2p$) and $(3, 1, 1, 0)$ closed core orbitals from (Zr: $4s, 4p$; O: $1s$) were selected. These orbitals were optimised for the $X^1\Sigma^+$, $A^1\Delta$, $B^1\Pi$, $C^1\Sigma^+$, $D^1\Gamma$, $F^1\Delta$, $a^3\Delta$, $b^3\Pi$, $c^3\Sigma^-$, $d^3\Phi$, $e^3\Pi$, $f^3\Delta$ and $(1)^3\Sigma^+$ electronic states with equal weighting. For the zirconium atom, a contracted version of the cc-pVTZ-PP basis set was employed in combination with the $2h$ function of the aug-cc-pVQZ-PP basis set ([Peterson et al. 2007](#)). The associated ECP28MDF effective core potential was used for the twenty-eight frozen electrons in the $1s^2 2s^2 2p^6 3s^2 3p^6 3d^{10}$ orbitals. The remaining twelve electrons in the $4s^2 4p^6 4d^2 5s^2$ orbitals were explicitly taken into the valence space. For the oxygen atom, a contracted version of the aug-cc-pVQZ basis set ([Kendall et al. 1992](#)) was used in an all electron scheme.

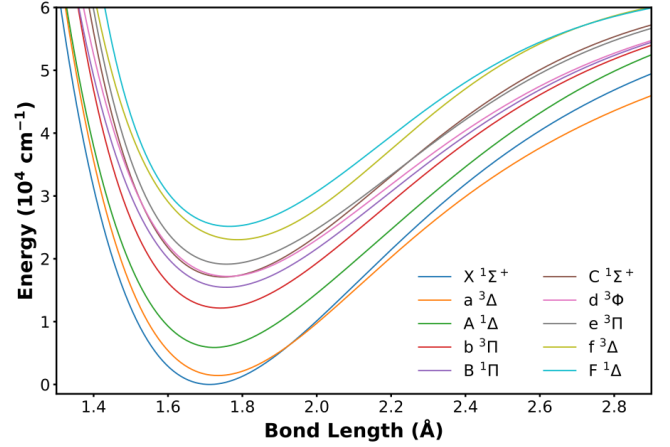


Figure 2. The ten ZrO electronic potential energy curves generated in this work. These were modelled using an extended Morse oscillator curve fit to the MARVEL experimental data.

3 $^{90}\text{Zr}^{16}\text{O}$ SPECTROSCOPIC MODEL

There is currently no available spectroscopic model ([McKemmish 2021](#)) (*i.e.* a set of self-consistent potential energy, coupling and dipole moment curves used in the variational model of a molecule) for $^{90}\text{Zr}^{16}\text{O}$ in the literature. The absence of this model hinders physically reasonable extrapolation of experimental data to new unobserved transitions.

Here, the $^{90}\text{Zr}^{16}\text{O}$ spectroscopic model is assembled for the ten $X^1\Sigma^+$, $a^3\Delta$, $A^1\Delta$, $b^3\Pi$, $B^1\Pi$, $C^1\Sigma^+$, $d^3\Phi$, $e^3\Pi$, $f^3\Delta$ and $F^1\Delta$ electronic states in a Duo ([Yurchenko et al. 2016](#)) .model input file. The $D^1\Gamma$, $E^1\Phi$ and $c^3\Sigma^-$ electronic states were excluded as there is no experimental data verifying their term energies and there are no allowed transitions with the low-lying $X^1\Sigma^+$ or $a^3\Delta$ electronic states.

3.1 Energy Spectroscopic Model

The $^{90}\text{Zr}^{16}\text{O}$ energy spectroscopic model comprises the potential energy curve of each electronic state, as well as the coupling and correction curves between these states. Firstly, the potential energy curves for the ten electronic states considered are shown in Figure 2, which were modelled using an extended Morse oscillator potential given by

$$V(R) = T_e + D_e \left[1 - \exp \left(\sum_{i=0}^N b_i \left(\frac{R^4 - R_e^4}{R^4 + R_e^4} \right)^i (R_e - R) \right) \right]^2 \quad (1)$$

where T_e is the term energy, D_e is the dissociation energy, R_e is the equilibrium bond length and $\{b_i\}$ are vibrational fitting parameters. The number of these fitting parameters differs on the left and right of the equilibrium bond length as specified by the parameters N_L and N_R in the .model input file, respectively. The dissociation asymptote $A_e = T_e + D_e$ was set to $7.89 \text{ eV} = 63,637 \text{ cm}^{-1}$ ([Murad & Hildenbrand 1975](#)) for all ten electronic states.

The ten potential energy curves were fit to 8,083 unique MARVEL experimental energies ([McKemmish et al. 2018](#)), where the inverse square of each MARVEL uncertainty was applied as the weighting factor in the fitting procedure. The degenerate MARVEL rovibronic states with unresolved Λ -doubling were duplicated with opposite parity for completeness. The *ab initio* potential energy curves from Section 2.3

Table 1. The fitted variational parameters of the potential energy and diagonal coupling curves for the X $^1\Sigma^+$, A $^1\Delta$, B $^1\Pi$, C $^1\Sigma^+$ and F $^1\Delta$ singlet electronic states. Apart from the dimensionless parameters N_L and N_R , all parameters are rounded to five significant figures in units of Å for R_e , Å $^{-i}$ for the b_i vibrational parameters and cm $^{-1}$ otherwise.

Parameter	X $^1\Sigma^+$	A $^1\Delta$	B $^1\Pi$	C $^1\Sigma^+$	F $^1\Delta$
T_e	+0.0000E+00	+5.8854E+03	+1.5458E+04	+1.7099E+04	+2.5156E+04
R_e	+1.7119E+00	+1.7243E+00	+1.7561E+00	+1.7492E+00	+1.7652E+00
A_e	+6.3637E+04	+6.3637E+04	+6.3637E+04	+6.3637E+04	+6.3637E+04
N_L	1	1	2	1	2
N_R	3	3	3	2	2
b_0	+1.7365E+00	+1.7653E+00	+1.7569E+00	+1.8300E+00	+1.9175E+00
b_1	+8.5932E-02	+1.2397E-01	+1.7479E-01	-7.3237E-02	+2.0378E-01
b_2	+5.5929E-02	-7.1092E-01	+1.2322E-01	+8.8427E-01	+1.0000E+00
b_3	-8.8825E-02	+1.0855E+00	+1.0925E-01	-	-
λ_q	-	-	+9.3589E-05	-	-

Table 2. The fitted variational parameters of the potential energy and diagonal coupling curves for the a $^3\Delta$, b $^3\Pi$, d $^3\Phi$, e $^3\Pi$ and f $^3\Delta$ triplet electronic states. Apart from the dimensionless parameters N_L and N_R , all parameters are rounded to five significant figures in units of Å for R_e , Å $^{-i}$ for the b_i vibrational parameters and cm $^{-1}$ otherwise.

Parameter	a $^3\Delta$	b $^3\Pi$	d $^3\Phi$	e $^3\Pi$	f $^3\Delta$
T_e	+1.4179E+03	+1.2159E+04	+1.7194E+04	+1.9146E+04	+2.3039E+04
R_e	+1.7343E+00	+1.7414E+00	+1.7604E+00	+1.7570E+00	+1.7869E+00
A_e	+6.3637E+04	+6.3637E+04	+6.3637E+04	+6.3637E+04	+6.3637E+04
N_L	1	2	1	1	2
N_R	3	2	2	2	2
b_0	+1.6856E+00	+1.7536E+00	+1.7844E+00	+1.7921E+00	+1.8178E+00
b_1	+6.5169E-02	+1.0791E-01	+1.0543E-01	-1.9849E-01	+5.5247E-01
b_2	+3.0025E-01	+2.7406E-01	+2.5423E-01	+9.5112E-01	+1.0000E+00
b_3	-6.6929E-01	-	-	-	-
A_{SO}	+3.1204E+02	-2.9868E+02	+6.1309E+02	-1.1935E+02	+3.6652E+02
λ_{SS}	-1.3596E+00	+1.1238E+01	+4.1128E+00	-8.5077E+00	+3.6586E+00
BO_{rot}	+6.7111E-03	+9.9077E-04	+1.0405E-02	+8.3545E-03	+1.1734E-02
γ_{SR}	-9.7375E-03	+2.6961E-01	+1.4856E+00	+2.7173E-01	+2.5983E+00
λ_{p2q}	-	+1.0989E-01	-	-	-
λ_{opq}	-	-1.7547E+01	-	-	-
λ_q	-	+1.1512E-04	-	-	-

were used to further confine the fit. The fitted parameters for each potential energy curve are provided in Tables 1 and 2.

Additionally, all spin-orbit (A_{SO}), spin-spin (λ_{SS}), spin-rotation (γ_{SR}), Λ -doubling (λ_{opq} , λ_{p2q} and λ_q), angular momentum (L_+) and Born-Oppenheimer breakdown (BO_{rot}) interactions were considered in this energy spectroscopic model. A constant value was utilised for these interactions across all bond lengths. For the off-diagonal spin-orbit and angular momenta curves, this constant value was set as its *ab initio* value at 1.71 Å, which is the equilibrium bond length of the ground X $^1\Sigma^+$ electronic state. The remaining values were fit using the MARVEL experimental data. The diagonal coupling parameters are provided in Tables 1 and 2 for all ten electronic states. The off-diagonal coupling parameters can be found in the Duo .model file.

Ultimately, the energy spectroscopic model constructed herein can accurately reproduce the MARVEL experimental energies for all ten electronic states. This is shown by the absolute energy residuals summarised statistically in Table 3, which were calculated as the absolute difference between the MARVEL experimental and variational energies.

In Table 4, the X $^1\Sigma^+$ and B $^1\Pi$ equilibrium spectroscopic parameters from this $^{90}\text{Zr}^{16}\text{O}$ model are compared to selected literature studies. There is a general agreement across all sources, with strong agreement to the MARVEL exper-

imental parameters (McKemmish et al. 2018) as expected from the fitting procedure. The greatest deviations are observed in comparison to the theoretical parameters (Langhoff & Bauschlicher 1990) as expected due to the inaccuracies of quantum chemistry in modelling complex transition metal diatomic molecules (Tennyson et al. 2016).

3.2 Intensity Spectroscopic Model

The $^{90}\text{Zr}^{16}\text{O}$ intensity spectroscopic model contains only *ab initio* dipole moment curves as is standard practice. These curves were inserted into the .model file without fitting to a functional form, where all interpolation was performed by Duo using natural splines. The intensity spectroscopic model includes all diagonal (permanent) and off-diagonal (transition) dipole moment curves shown in Figures 3 and 4, respectively. The latter also includes values calculated by Langhoff & Bauschlicher (1990) for various off-diagonal curves.

The *ab initio* dipole moment curves in Figures 3 and 4 are exceptional for a transition metal diatomic molecule. Importantly, all curves are smooth and well-defined around the equilibrium bond length of each electronic state. Apart from the f $^3\Delta$ electronic state, all diagonal dipole moment curves follow the same pattern as they tend towards zero. The f $^3\Delta$ diagonal curve likely approaches zero beyond 5 Å. Similarly,

Table 3. A statistical summary of the $^{90}\text{Zr}^{16}\text{O}$ absolute energy residuals grouped by electronic state for each vibrational state v in the MARVEL analysis. The root mean square error (RMSE), mean absolute error (MAE) and maximum residual are presented for each vibronic level in units of cm^{-1} .

State	v	RMSE	MAE	Maximum
X $^1\Sigma^+$	0	1.059E-01	9.233E-02	2.737E-01
	1	9.139E-02	8.528E-02	1.762E-01
	2	1.450E-01	1.402E-01	2.717E-01
	3	1.271E-01	1.217E-01	2.894E-01
	4	9.591E-02	8.155E-02	2.546E-01
	5	6.058E-02	4.363E-02	2.596E-01
	6	1.203E-01	1.020E-01	2.750E-01
7	2.229E-01	2.131E-01	3.361E-01	
a $^3\Delta$	0	8.433E-01	4.567E-01	4.593E+00
	1	8.138E-01	6.033E-01	4.086E+00
	2	8.516E-01	6.148E-01	4.115E+00
	3	7.107E-01	6.083E-01	2.433E+00
	4	9.587E-01	8.011E-01	1.834E+00
5	1.395E+00	1.105E+00	2.423E+00	
A $^1\Delta$	0	2.576E-01	2.115E-01	5.842E-01
	1	5.576E-01	4.065E-01	1.905E+00
b $^3\Pi$	0	1.099E-01	7.866E-02	4.417E-01
B $^1\Pi$	0	3.685E-02	2.706E-02	1.645E-01
	1	3.819E-02	2.657E-02	1.746E-01
	2	9.147E-02	5.152E-02	6.875E-01
	3	6.511E-02	4.658E-02	2.959E-01
	4	5.177E-02	3.980E-02	1.864E-01
5	7.217E-02	5.803E-02	1.988E-01	
C $^1\Sigma^+$	0	7.253E-02	5.394E-02	2.160E-01
d $^3\Phi$	0	2.426E+00	2.040E+00	7.437E+00
	1	1.639E+00	1.355E+00	5.863E+00
	2	6.627E-01	3.900E-01	3.734E+00
	3	1.222E+00	1.041E+00	3.169E+00
4	3.172E+00	2.897E+00	5.189E+00	
e $^3\Pi$	0	8.022E-01	5.677E-01	3.049E+00
f $^3\Delta$	0	1.291E+00	9.774E-01	3.444E+00
F $^1\Delta$	0	3.868E-01	3.400E-01	8.467E-01
	1	5.116E-01	4.338E-01	1.001E+00

the off-diagonal dipole moment curves generally converge to zero. These off-diagonal curves are consistent with the values calculated by Langhoff & Bauschlicher (1990) around the equilibrium bond length. The off-diagonal dipole moment curves associated with the $f^3\Delta$ electronic state again likely tend towards zero beyond 5 Å. The high $f^3\Delta$ dipole moment values around 4 Å may be due to a remaining predominant ionic behaviour before reaching the neutral fragment at the dissociation. Nevertheless, it was found that the vibrational basis functions generated by Duo have negligible amplitude beyond 2.5 Å for all electronic states. This eliminates the need for these *ab initio* curves beyond this bond length.

4 ZrO LINE LIST CONSTRUCTION

4.1 Methodology Overview

The line list construction approach of Syme & McKemmish (2021) is followed herein for ZrO, where the MARVEL exper-

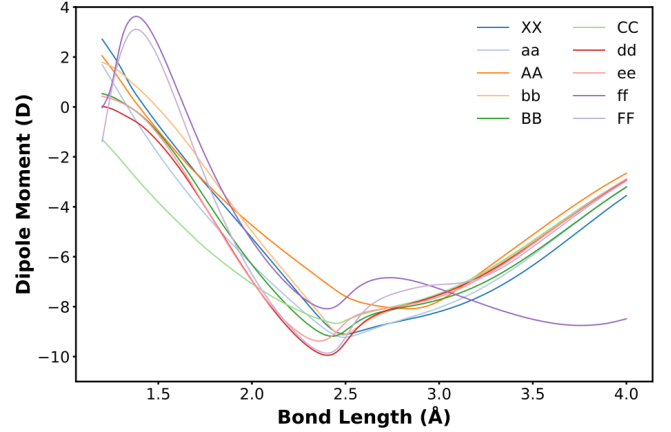


Figure 3. The $^{90}\text{Zr}^{16}\text{O}$ diagonal (permanent) dipole moment curves as obtained from *ab initio* calculations.

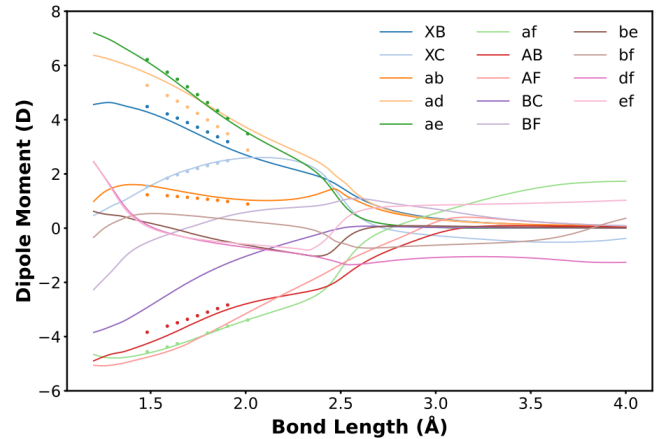


Figure 4. The $^{90}\text{Zr}^{16}\text{O}$ (transition) off-diagonal dipole moment curves as obtained from *ab initio* calculations, which were transformed into the Duo Λ -representation. The coloured dots indicate values calculated by Langhoff & Bauschlicher (1990) in the Cartesian representation, where the $\Delta - \Pi$ and $\Phi - \Delta$ curves were scaled by $\sqrt{2}$ to convert between real and complex orbitals.

imental, MoLLIST perturbative and Duo variational energies are collated into a trihybrid line list. This methodology exploits the advantages of each methodology to produce the most accurate and comprehensive line list for ZrO.

In accordance with ExoMol line lists conventions, a trihybrid line list is prepared by updating the energies of the variational .states file. The trihybrid methodology prioritises the experimental energies due to their superior accuracy and reliable uncertainties. These replace the variational energies wherever possible with subsequent interpolation by the perturbative energies. The final trihybrid .states file includes the methodology and variational energy of each state, where the abbreviations Ma, EH and Ca represent the experimental (MARVEL), perturbative (effective Hamiltonian) and variational (calculated) methodologies, respectively.

The $^{90}\text{Zr}^{16}\text{O}$ variational line list is output directly from Duo using the energy and intensity spectroscopic model detailed in Section 3. The quantum numbers are given in terms of Hund's coupling case (a). The $^{90}\text{Zr}^{16}\text{O}$ trihybrid line list was created by replacing the variational energies with MAR-

Table 4. The $^{90}\text{Zr}^{16}\text{O}$ equilibrium spectroscopic parameters from selected sources reported without error estimates in units of \AA for R_e and cm^{-1} otherwise. The theoretical parameters from Langhoff & Bauschlicher (1990) are obtained from the MRCI calculations.

State	Parameter	ZORRO	H & H (1979)	MARVEL	MoLLIST	L & B (1990)
X $^1\Sigma^+$	A_e	63,637	63,315	–	–	–
	R_e	1.7119	1.7116	–	1.71199404	1.721
	ω_e	976.16	969.76	976.44	976.40869	979.1
	$\omega_e x_e$	3.3758	4.90	3.45	3.44153	–
	B_e	0.42361	0.42263	0.42361	0.4235669	–
	D_e (10^{-7})	3.19	3.19	3.19	–	–
	α_e (10^{-3})	1.9572	2.3	1.97	1.9186	–
	T_e	15,458	15,443	15,441.70	–	15,168
B $^1\Pi$	A_e	63,637	–	–	–	–
	R_e	1.7561	1.75832	–	1.75631230	1.756
	ω_e	859.35	859	859.59	859.424252	899.9
	$\omega_e x_e$	2.9669	3	2.99	2.921697	–
	B_e	0.402576	0.40154	0.40246	0.402460322	–
	D_e (10^{-7})	3.53	3.52	3.50	–	–
	α_e (10^{-3})	1.9092	–	1.90	1.8770	–

Table 5. An extract from the $^{90}\text{Zr}^{16}\text{O}$.states file. The total file is available at www.exomol.com and in the supplementary material.

n	\tilde{E}	g_{tot}	J	unc	τ	g	$p_{+/-}$	$p_{e/f}$	State	v	Λ	Σ	Ω	Source	\tilde{E}_{Ca}
5633	18746.741719	13	6	9.2000E+00	2.3475E-03	9.4090E-02	–	f	a3Delta	20	-2	0	-2	Ca	18746.741719
5634	18778.561300	13	6	5.8000E-02	6.4538E-08	2.3798E-02	–	f	B1Pi	4	-1	0	-1	EH	18778.515781
5635	18817.703605	13	6	1.2000E-02	3.9329E-08	2.1485E-01	–	f	d3Phi	2	-3	0	-3	Ma	18817.782124

Table 6. The column descriptors of the ZrO .states files. Here, \hat{L} is the electronic orbital angular momentum, \hat{S} is the electronic spin angular momentum and \hat{J} is the total angular momentum excluding nuclear spin angular momentum (Tennyson et al. 2016).

Column	Symbol	Descriptor
1	n	State Index
2	\tilde{E}	Energy (in cm^{-1})
3	g_{tot}	Total Degeneracy
4	J	Total Angular Momentum
5	unc	Uncertainty (in cm^{-1})
6	τ	Lifetime (in s)
7	g	Landé g -Factor
8	$p_{+/-}$	Total Parity
9	$p_{e/f}$	Rotationless Parity
10	State	Electronic State
11	v	Vibrational State
12	Λ	\hat{L} Projection Along Internuclear Axis
13	Σ	\hat{S} Projection Along Internuclear Axis
14	Ω	\hat{J} Projection Along Internuclear Axis (with $\Omega = \Lambda + \Sigma$)
15	Source	State Source (Ma, EH or Ca)
16	\tilde{E}_{Ca}	Variational Energy (in cm^{-1})

Table 7. An extract from the $^{90}\text{Zr}^{16}\text{O}$.trans file. The total file is available at www.exomol.com and in the supplementary material.

f	i	A_{fi}
391	1	4.7878E-07
392	1	9.9341E+00
393	1	2.5024E-02

Table 8. The column descriptors of the ZrO .trans files.

Column	Symbol	Descriptor
1	f	Final State Index
2	i	Initial State Index
3	A_{fi}	Einstein A Coefficient (in s^{-1})

VEL experimental energies (McKemmish et al. 2018) where available, followed by interpolation MoLLIST perturbative energies (Sorensen & Bernath 2021) to cover any missing experimental data. These energy replacements were performed using an external Python script by grouping equivalent rovibronic states from each source by their electronic state, parity, J , v and Ω quantum numbers.

For all other isotopologues, a variational line list can be constructed trivially by changing the nuclear masses in the main spectroscopic model. Following Polyansky et al. (2017), the accuracy of this line list can be improved by applying an isotopologue extrapolation term that shifts each energy based on the difference between the variational and trihybrid line lists of the main $^{90}\text{Zr}^{16}\text{O}$ isotopologue as

$$\tilde{E}_{\text{IE}}^{\text{iso}} = \tilde{E}_{\text{Ca}}^{\text{iso}} + \left(\tilde{E}_{\text{tri}}^{\text{main}} - \tilde{E}_{\text{Ca}}^{\text{main}} \right) \quad (2)$$

where $\tilde{E}_{\text{Ca}}^{\text{main}}$ is the calculated variational energy of the main isotopologue, $\tilde{E}_{\text{tri}}^{\text{main}}$ is its trihybrid energy, $\tilde{E}_{\text{Ca}}^{\text{iso}}$ is the calculated variational energy of a given isotopologue and $\tilde{E}_{\text{IE}}^{\text{iso}}$ is its isotopologue-extrapolated energy. In other words, it is assumed that the energy residuals between the hybridised and variational line lists are constant for all isotopologues.

4.2 Line List Overview

The ZORRO trihybrid .states file contains 227,118 rovibronic states with 13,075 (7,769 unique) experimental states, 106 perturbative states and 213,937 variational states. These were calculated up to the dissociation limit of $63,637 \text{ cm}^{-1}$, although the electronic structure of ZrO is poorly understood above $30,000 \text{ cm}^{-1}$ (McKemmish et al. 2018). An extract of the final .states files is shown Table 5 with associated column descriptors in Table 6.

The ZORRO trihybrid .trans file contains 47,662,773 transitions. A maximum transition frequency threshold of

Table 9. The partition functions for ZrO as a function of temperature T (in K) from different sources. The left section compares values for the main $^{90}\text{Zr}^{16}\text{O}$ isotopologue and the right section gives values for the five other isotopologues considered in this work.

T (K)	$^{90}\text{Zr}^{16}\text{O}$	MARVEL	B & C (2016)	$^{91}\text{Zr}^{16}\text{O}$	$^{92}\text{Zr}^{16}\text{O}$	$^{93}\text{Zr}^{16}\text{O}$	$^{94}\text{Zr}^{16}\text{O}$	$^{96}\text{Zr}^{16}\text{O}$
0	1.00000E+00	1.00000E+00	1.00000E+00	6.00000E+00	1.00000E+00	6.00000E+00	1.00000E+00	1.00000E+00
1	2.02450E+00	2.02446E+00	2.02843E+00	1.21627E+01	2.02970E+00	1.21936E+01	2.03480E+00	2.03970E+00
10	1.68071E+01	1.68071E+01	1.68283E+01	1.01007E+02	1.68614E+01	1.01327E+02	1.69137E+01	1.69642E+01
100	1.64881E+02	1.64881E+02	1.65280E+02	9.90930E+02	1.65423E+02	9.94124E+02	1.65946E+02	1.66450E+02
300	5.06399E+02	5.06325E+02	5.07801E+02	3.04356E+03	5.08103E+02	3.05359E+03	5.09746E+02	5.11330E+02
500	1.00696E+03	1.00632E+03	1.01006E+03	6.05271E+03	1.01057E+03	6.07397E+03	1.01405E+03	1.01741E+03
800	2.51223E+03	2.50894E+03	–	1.51030E+04	2.52201E+03	1.51606E+04	2.53144E+03	2.54054E+03
1,000	4.19424E+03	4.18561E+03	4.20923E+03	2.52168E+04	4.21119E+03	2.53167E+04	4.22754E+03	4.24333E+03
1,500	1.11864E+04	1.10826E+04	1.12345E+04	6.72634E+04	1.12343E+04	6.75461E+04	1.12806E+04	1.13253E+04
2,000	2.25679E+04	2.18849E+04	2.26794E+04	1.35711E+05	2.26679E+04	1.36300E+05	2.27645E+04	2.28577E+04
3,000	6.02447E+04	5.32615E+04	6.06178E+04	3.62304E+05	6.05206E+04	3.63930E+05	6.07869E+04	6.10441E+04
5,000	2.10516E+05	1.36797E+05	2.14087E+05	1.26600E+06	2.11476E+05	1.27166E+06	2.12401E+05	2.13295E+05

30,000 cm^{-1} was applied as this range is suitable for most telescopes and ensures that the $X^1\Sigma^+$ and a $^3\Delta$ bands are reliable. These transitions were only calculated for states with lower energy below 20,000 cm^{-1} given that this contains 99.999% of the total population at 2,000 K according to the Boltzmann distribution. A vibrational basis set up to $v = 30$ was used for each electronic state with rotational states calculated to $J = 200$. An extract of the final .trans files is shown Table 7 with associated column descriptors in Table 8. Additionally, isotopologue-extrapolated hybrid line lists were prepared for $^{91}\text{Zr}^{16}\text{O}$, $^{92}\text{Zr}^{16}\text{O}$, $^{93}\text{Zr}^{16}\text{O}$, $^{94}\text{Zr}^{16}\text{O}$ and $^{96}\text{Zr}^{16}\text{O}$ using the technique in Section 4.1.

4.3 Uncertainties

The uncertainties assigned to the experimental, perturbative and variational energies were all evaluated differently.

For the main $^{90}\text{Zr}^{16}\text{O}$ isotopologue, the experimental uncertainties were obtained directly from the MARVEL analysis. The perturbative uncertainties were averaged from the experimental uncertainties with the same vibrational and rotational quantum numbers, where the experimental and perturbative energies are known to have similar accuracy when interpolating. The variational uncertainties were approximated using the energy residuals in Table 3. For energies within a vibrational state in the MARVEL analysis, the uncertainty is given as the largest energy residual with the same vibrational quantum number. For energies within a vibrational state unknown by the MARVEL analysis, the uncertainty is given as twice the largest energy residual in the same electronic state. All uncertainties were rounded to two significant figures.

For the five other isotopologues, all uncertainties were doubled to account for errors arising from the isotopologue-extrapolation technique.

5 ZrO LINE LIST ANALYSIS

ExoCross (Yurchenko et al. 2018) was used to generate partition functions, lifetimes and cross sections for all six ZrO isotopologues studied here.

5.1 Partition Functions

The partition functions $Q(T)$ were calculated using

$$Q(T) = \sum_n g_n^{\text{ns}} (2J_n + 1) e^{-c_2 \tilde{E}_n / T} \quad (3)$$

where g^{ns} is the nuclear spin statistical weight factor, J is the total angular momentum excluding nuclear spin, $c_2 = hc/k_B$ (in cm K), \tilde{E} is the energy term value (in cm^{-1}), and T is temperature (in K).

In Table 9, the six partition functions are evaluated at selected temperatures. For $^{90}\text{Zr}^{16}\text{O}$, the partition function is compared to values calculated by McKemmish et al. (2018) and Barklem & Collet (2016). There is strong agreement between the ZORRO data and Barklem & Collet (2016), even at 5,000 K, thus strongly corroborating both data sets. The MARVEL-only data are surprisingly complete to 2,000 K, although the lack of vibrational states results in an underestimation of the partition function at higher temperatures.

5.2 Lifetimes

The lifetime τ_i of each rovibronic state is calculated as

$$\tau_i = \frac{1}{\sum_f A_{fi}} \quad (4)$$

where A_{fi} are Einstein A coefficients.

In Table 10, selected excited vibronic lifetime of $^{90}\text{Zr}^{16}\text{O}$ are presented as averaged over all rotational states with $J \leq 10$ with $|\Omega|$ -resolution. For three electronic states, the vibronic lifetimes of ZORRO can be compared to experimental values from Hammer & Davis (1979) and Simard et al. (1988); this comparison provides the best experimental validation of the computed off-diagonal (transition) dipole moments. The $C^1\Sigma^+$ state agreement is exceptional. The $B^1\Pi$ and $e^3\Pi$ state theory-experiment agreement is reasonable, with our new theoretical predictions slightly closer to experimental data than the earlier theoretical calculations.

These vibronic lifetimes are also compared to theoretical values from Langhoff & Bauschlicher (1990), with typically strong agreement as expected given the similarity in the dipole moment curves. The largest error is for the $b^3\Pi$ lifetime, which is unexpected since the dominant contribution, the $b^3\Pi - a^3\Delta$ dipole moment curve, is almost identical. This was investigated to ensure the correct conversion from Molpro output to Duo input was performed, but the cause of this discrepancy could not be identified. It should be noted that the $e^3\Pi - a^3\Delta$ transition was treated in the same way, resulting in $e^3\Pi$ lifetimes very similar to Langhoff & Bauschlicher (1990) and close to experimental data. Any $b^3\Pi$ experimental lifetimes will thus be helpful here.

Table 10. The excited vibronic lifetimes τ (in ns) of $^{90}\text{Zr}^{16}\text{O}$ with $|\Omega|$ -resolution averaged over all rotational states with $J \leq 10$.

State	v	$ \Omega $	ZORRO	L & B (1990)	Experiment
b $^3\Pi$	0	0	1580	1070 ^a	–
	0	1	1630	1070 ^a	–
	0	2	1720	1070 ^a	–
B $^1\Pi$	0	1	62.9	56.4	83 ^{ac}
C $^1\Sigma^+$	0	0	130	136	126(9) ^{ac}
d $^3\Phi$	0	2	40.3	45.9 ^a	–
	0	3	38.1	45.9 ^a	–
	0	4	35.8	45.9 ^a	–
e $^3\Pi$	0	0	25.5	24.4 ^a	32.5(2) ^{ab}
	0	1	26.4	24.4 ^a	32.5(2) ^{ab}
	0	2	27.3	24.4 ^a	32.5(2) ^{ab}
f $^3\Delta$	0	1	21.7	28.3 ^a	–
	0	2	21.8	28.3 ^a	–
	0	3	21.5	28.3 ^a	–

a No $|\Omega|$ -resolution provided.

b The experimental lifetime for $v' = 0$, $J' = 77$ from [Hammer & Davis \(1979\)](#). The equivalent ZORRO lifetime is $\tau = 27.4$ ns when averaged over all fine structure.

c The experimental lifetimes for $v' = 0$ from [Simard et al. \(1988\)](#).

5.3 Cross Sections

Here, cross sections are presented for the main $^{90}\text{Zr}^{16}\text{O}$ isotopologue only. The absorption cross sections in Figures 5, 6 and 7 were simulated using a Gaussian lineshape with a half-width at half-maximum of 2 cm^{-1} . The emission cross section in Figure 8 was simulated using a half-width at half-maximum of 0.1 cm^{-1} to replicate the laboratory spectrum.

In Figure 5, the total $^{90}\text{Zr}^{16}\text{O}$ absorption cross section at 2,000 K is decomposed into its primary transition bands for $0 - 30,000\text{ cm}^{-1}$. The spectrum possesses many intense transitions in all spectral regions. The visible region is the most prominent, where the B $^1\Pi - X^1\Sigma^+$, α ($f^3\Delta - a^3\Delta$), β ($e^3\Pi - a^3\Delta$), γ ($d^3\Phi - a^3\Delta$) transitions dominate.

In Figure 6, the total $^{90}\text{Zr}^{16}\text{O}$ absorption cross section at 2,000 K is generated using three line lists. The black, blue and orange cross sections indicate transitions provided by the trihybrid, MARVEL experimental (with variational intensities) and MoLLIST perturbative line lists, respectively. As expected, the trihybrid line list produces the most comprehensive cross section due to its inclusion of the variational transition intensities calculated in this work. The MARVEL analysis offers good coverage in the visible and near-infrared spectral regions corresponding to the major B $^1\Pi - X^1\Sigma^+$, α , β and γ rovibronic transitions. The MoLLIST cross section is only present for the B $^1\Pi - X^1\Sigma^+$ transition. Evidently, the MoLLIST line list can not sufficiently model the total $^{90}\text{Zr}^{16}\text{O}$ absorption cross section given that it does not account for many other overlapping transitions.

In Figure 7, the total $^{90}\text{Zr}^{16}\text{O}$ absorption cross section is simulated at several temperatures. The weaker bands in the cross section increase in intensity and become less defined with increasing temperature.

In Figure 8, the $^{90}\text{Zr}^{16}\text{O}$ emission cross section simulated from the trihybrid line list is compared with an experimental emission spectrum for $14,000 - 17,000\text{ cm}^{-1}$, which was recorded at 2,390 K with a resolution of 0.04 cm^{-1} and was

used in the perturbative analysis of [Sorensen & Bernath \(2021\)](#). As expected, the transition frequencies are in excellent agreement between both spectra, including for many weaker bands. The transition intensities from the trihybrid line list provide an accurate description of the experimental spectrum, which supports the off-diagonal dipole moment curves in Figure 4. Overall, this comparison is a good improvement over an analogous figure provided by [Sorensen & Bernath \(2021\)](#) using their B $^1\Pi - X^1\Sigma^+$ line list.

5.4 High-Resolution Considerations

In order to assess the suitability of a line list for use in the high-resolution cross-correlation (abbreviated as HRCC) detection of a molecule, it is critical to know the accuracy with which line positions are known. The accuracy of a transition frequency depends on the source of the energies of its upper and lower state. If both the upper and lower state energies are known from MARVEL data (with typically low uncertainties), then its frequency can be assumed to be known to high accuracy. Conversely, if one or both of the energy levels are calculated from the Duo variational spectroscopic model, then the frequency will have much higher uncertainty; it is assumed here that it is insufficiently accurate for HRCC studies. The effective Hamiltonian perturbative data can be neglected from this discussion due to the low number of energies in the ZORRO line list.

Again, in Figure 6, the cross section of the full ZORRO trihybrid line list (assumed to be near complete based on partition function considerations and the inclusion of all predicted low-lying electronic states) is compared with the cross section predicted solely by MARVEL data (assumed to be highly accurate). In spectral regions where the two curves overlap, it should be understood that the transition frequency of the strong line is predicted to experimental (MARVEL) accuracy. In this case, Figure 6 shows that the ZORRO trihybrid line list is suitable for HRCC primarily between $12,500 - 17,500\text{ cm}^{-1}$ ($571 - 800\text{ nm}$) at 2,000 K, but not in most other spectral regions. Fortunately, this region is typically quite experimentally accessible. It should be noted that this figure can be readily generated at different temperatures using ExoCross and examined at higher resolutions to ensure suitability for a desired application.

Additionally, Figure 6 clearly demonstrates the challenges one might face using the previous [Sorensen & Bernath \(2021\)](#) data alone for HRCC. Narrow spectral windows would be needed, often undesirable as they reduce signal strength. Further, the $d^3\Phi - a^3\Delta$ band (not present in this earlier data) overlaps almost entirely with the well-predicted B $^1\Pi - X^1\Sigma^+$ band; cross-correlation using the [Sorensen & Bernath \(2021\)](#) as template data would therefore utilise fewer lines and thus require a much higher signal-to-noise observational data for detection than cross-correlation using our new ZORRO line list data.

A useful complementary perspective on high-resolution completeness is obtained from Figure 9. This plot is read by looking at vertical slices to visualise the source of upper and lower state energies for transitions above that intensity. For example, the vertical slice at $10^{-18}\text{ cm molecule}^{-1}$ shows that about half of all transitions with intensity greater than $10^{-18}\text{ cm molecule}^{-1}$ have both upper and lower energies from the high-resolution MARVEL/MoLLIST data; this means that

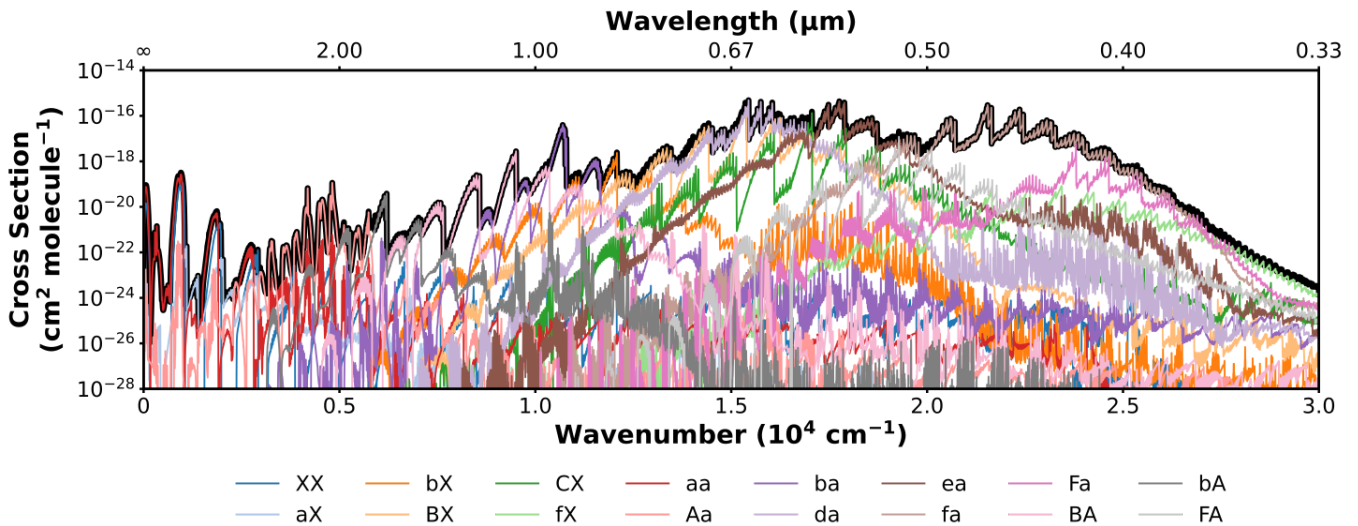


Figure 5. The total $^{90}\text{Zr}^{16}\text{O}$ absorption cross section decomposed at 2,000 K for 0 – 30,000 cm^{-1} .

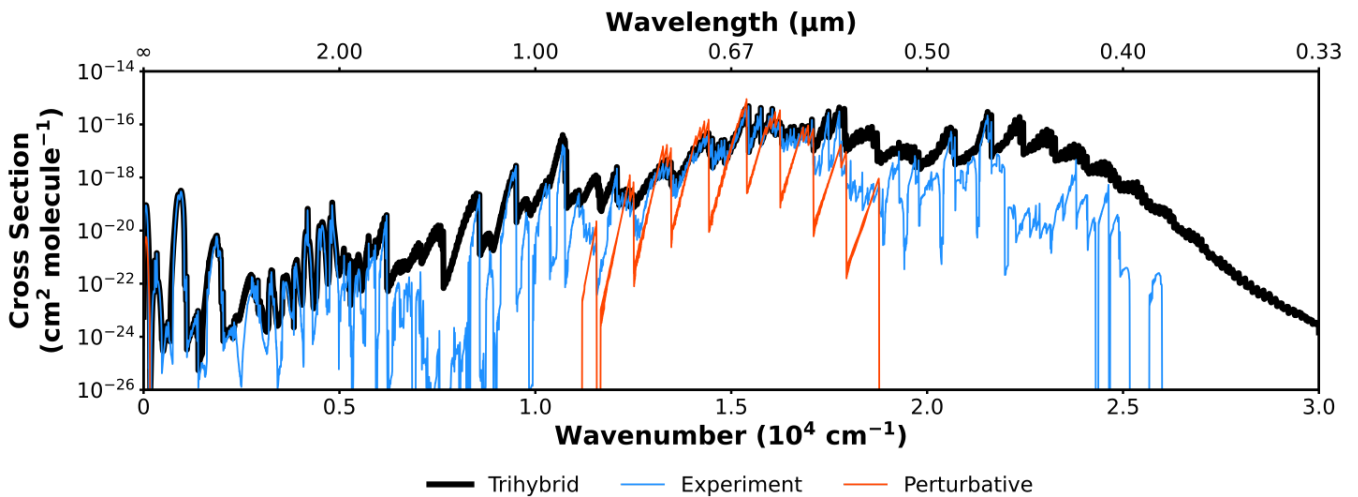


Figure 6. The total $^{90}\text{Zr}^{16}\text{O}$ absorption cross section simulated at 2,000 K from different sources. The black, blue and orange cross sections show transitions accounted for by the ZORRO trihybrid line list, MARVEL experimental line list by McKemmish et al. (2018) (with variational intensities) and MoLLIST perturbative line list by Sorensen & Bernath (2021), respectively.

the ZORRO line list cannot be trusted to accurately predict about half of all transitions with strength above 10^{-18} $\text{cm}^2 \text{ molecule}^{-1}$ at 2,000 K. This statistic emphasises the importance of carefully selecting the spectral range for HRCC in ZrO. For molecules with sufficient MARVEL data, there is thus expected to be fewer restrictions on the spectral regions suitable for HRCC detections.

In order to improve the high-resolution completeness of the ZORRO trihybrid line list for HRCC studies, the $^{90}\text{Zr}^{16}\text{O}$ MARVEL analysis would need to be expanded with new experimental data. The most important gaps are the $e^3\Pi$ and $f^3\Delta$ electronic states, which will enable accuracy at shorter wavelengths than currently possible, while the $b^3\Pi$ electronic state would be useful for longer wavelength studies.

6 CONCLUSIONS AND FUTURE DIRECTIONS

Modern searches for molecules like ZrO rely on both traditional mid-resolution space-based observations (such as from JWST) and very high-resolution ground-based observations (such as from ESPRESSO/VLT). In order to enable the former and thus successfully model complex physical and chemical processes in astronomical bodies, experience has shown that a high coverage of absorption lines across a wide temperature and spectral range is important (Fortenberry 2017; Tennyson & Yurchenko 2012). In contrast, to enable molecule detection using the modern high-resolution cross-correlation spectroscopic technique, line positions for strong lines must be accurate to about 0.1 cm^{-1} over the desired spectral region; astronomers should select spectral regions based on the accuracy of the best available line lists.

Therefore, the joint goals of accuracy and completeness are achieved by carefully combining experimental data (to provide high accuracy) with computational models (to pro-

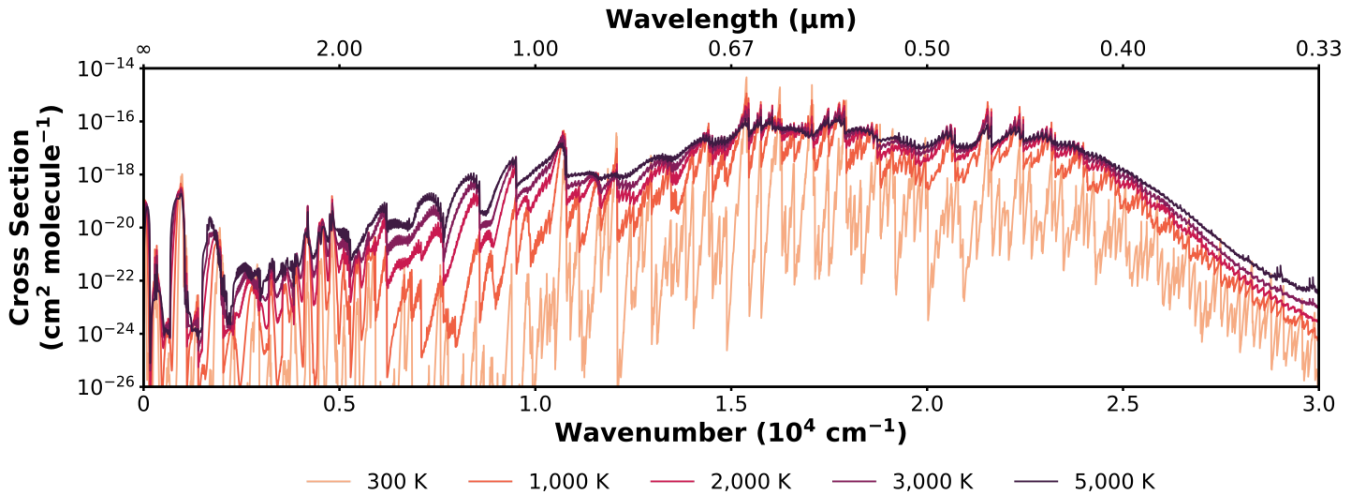


Figure 7. The total $^{90}\text{Zr}^{16}\text{O}$ absorption cross section simulated at several temperatures.

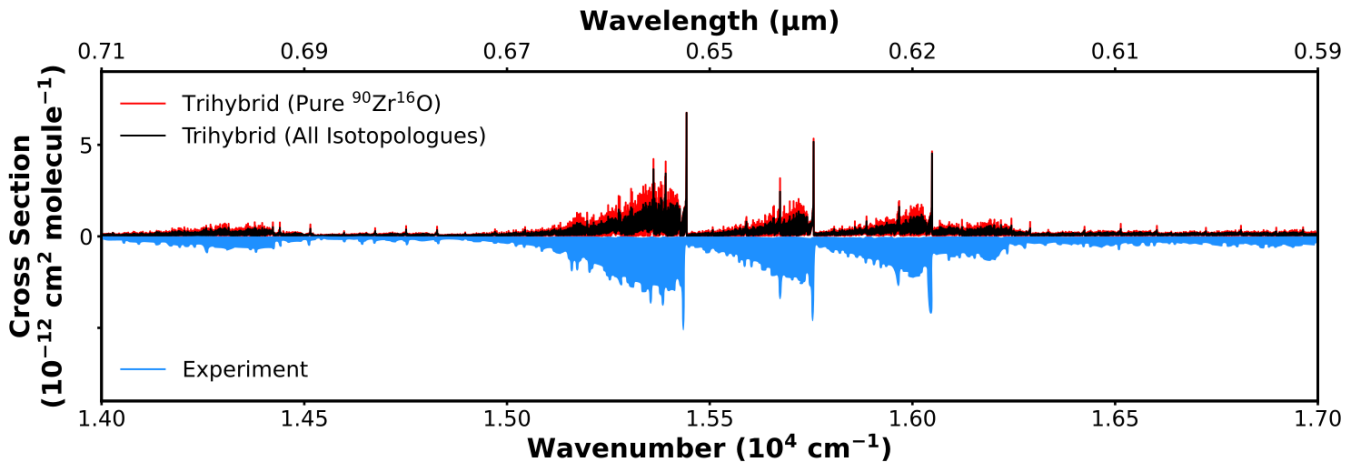


Figure 8. A comparison of the ZrO emission cross section simulated from the trihybrid line list with an experimental spectrum at 2,390 K for 14,000 – 17,000 cm^{-1} . The red trihybrid cross section was generated using only the main $^{90}\text{Zr}^{16}\text{O}$ isotopologue, whereas the black trihybrid cross section was generated using all six isotopologues scaled in accordance with their zirconium isotopic abundance. The experimental cross section was obtained from [Sorensen & Bernath \(2021\)](#) and copied over the trihybrid cross sections.

vide high completeness). In the construction of the ZORRO trihybrid line list for ZrO, experimental data are combined with data generated from perturbative (effective Hamiltonians) and variational models. The novel spectroscopic model presented herein considered the ten low-lying $X^1\Sigma^+$, $a^3\Delta$, $A^1\Delta$, $b^3\Pi$, $B^1\Pi$, $C^1\Sigma^+$, $d^3\Phi$, $e^3\Pi$, $f^3\Delta$ and $F^1\Delta$ electronic states of ZrO.

Through the trihybrid methodology, the ZORRO line list is now the most accurate and comprehensive line list available for ZrO. Line lists are available for the main $^{90}\text{Zr}^{16}\text{O}$ isotopologue, as well as the $^{91}\text{Zr}^{16}\text{O}$, $^{92}\text{Zr}^{16}\text{O}$, $^{93}\text{Zr}^{16}\text{O}$, $^{94}\text{Zr}^{16}\text{O}$ and $^{96}\text{Zr}^{16}\text{O}$ isotopologues. This new data can be reliably used for molecular detections using high-resolution cross-correlation techniques in the 12,500 – 17,500 cm^{-1} (571 – 800 nm) spectral region, but should not be used at other wavelengths due to the insufficiently complete experimental data. Studies of other vibronic bands of the $B^1\Pi - X^1\Sigma^+$ and $b^3\Pi - a^3\Delta$ transitions would enable use of high-resolution techniques in a wider spectral region.

ACKNOWLEDGEMENTS

This research was undertaken with the assistance of resources from the National Computational Infrastructure (NCI Australia), an NCRIS enabled capability supported by the Australian Government.

The authors declare no conflicts of interest.

DATA AVAILABILITY STATEMENT

All line list data for this article are available on the ExoMol website, specifically:

- The main ZORRO .model file (90Zr16O_ZorrO.model).
- The main ZORRO partition function from 0 – 10,000 K (90Zr16O_ZorrO.pf).
- The main ZORRO .states file (90Zr16O_ZorrO.states).
- The main ZORRO .trans file (90Zr16O_ZorrO.trans).

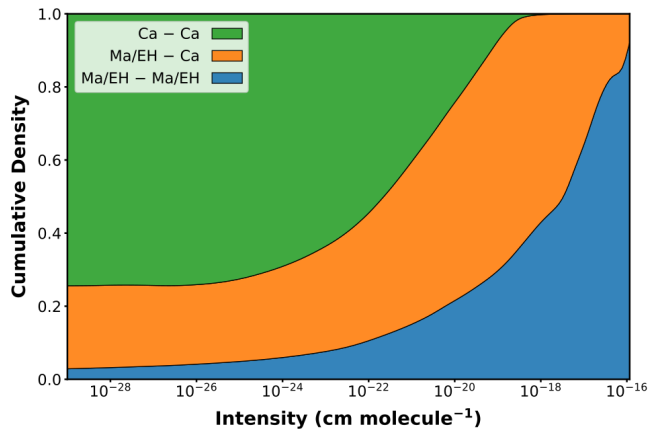


Figure 9. The cumulative density of energy sources as a function of transition intensity. The abbreviations Ma, EH and Ca represent the experimental (MARVEL), perturbative (effective Hamiltonian) and variational (calculated) methodologies, respectively.

- All other isotopologue .model, .pf, .states and .trans files (in their respective folders).

The Duo spectroscopic model, partition function and .states files for the main $^{90}\text{Zr}^{16}\text{O}$ isotopologue are included as supporting information for this paper. The Molpro quantum chemistry input files are also included for the MRCI calculations.

REFERENCES

Barklem P. S., Collet R., 2016, *Astronomy and Astrophysics*, 588
 Bernath P. F., 2020, *Journal of Quantitative Spectroscopy and Radiative Transfer*, 240, 106687
 Birkby J. L., 2018, Spectroscopic Direct Detection of Exoplanets. Springer International Publishing, Cham, pp 1485–1508, doi:10.1007/978-3-319-55333-7_16, https://doi.org/10.1007/978-3-319-55333-7_16
 Bobrovnikoff N. T., 1934, *The Astrophysical Journal*, 79, 483
 Borsa F., et al., 2021, *Astronomy and Astrophysics*, 645
 Brogi M., Line M. R., 2018, *The Astronomical Journal*, 157, 114
 Fortenberry R. C., 2017, *International Journal of Quantum Chemistry*, 117, 81
 Furtenbacher T., Császár A. G., Tennyson J., 2007, *Journal of Molecular Spectroscopy*, 245, 115
 Hammer P. D., Davis S. P., 1979, *Journal of Molecular Spectroscopy*, 78, 337
 Huber K. P., Herzberg G., 1979, *Molecular Spectra And Molecular Structure, IV. Constants Of Diatomic Molecules*
 Keenan P. C., 1954, *The Astrophysical Journal*, 120, 484

Keenan P. C., Boeshaar P. C., 1980, *The Astrophysical Journal Supplement Series*, 43, 379
 Kendall R. A., Dunning T. H., Harrison R. J., 1992, *The Journal of Chemical Physics*, 96, 6796
 Landman R., Sánchez-López A., Mollière P., Kesseli A. Y., Louca A. J., Snellen I. A., 2021, *Astronomy and Astrophysics*, 656
 Langhoff S. R., Bauschlicher C. W., 1990, *The Astrophysical Journal*, 349, 369
 McKemmish L. K., 2021, *WIREs Computational Molecular Science*, 11
 McKemmish L. K., et al., 2018, *The Astrophysical Journal*, 867, 33
 McKemmish L. K., Masseron T., Hoeijmakers H. J., Pérez-Mesa V., Grimm S. L., Yurchenko S. N., Tennyson J., 2019, *Monthly Notices of the Royal Astronomical Society*, 488, 2836
 Murad E., Hildenbrand D. L., 1975, *The Journal of Chemical Physics*, 63, 1133
 Nomura M., Kogure K., Okamoto M., 1983, *International Journal of Mass Spectrometry and Ion Physics*, 50, 219
 Nugroho S. K., Kawahara H., Masuda K., Hirano T., Kotani T., Tajitsu A., 2017, *The Astronomical Journal*, 154, 221
 Peterson K. A., Figgen D., Dolg M., Stoll H., 2007, *Journal of Chemical Physics*, 126
 Piccirillo J., 1980, *Monthly Notices of the Royal Astronomical Society*, 190, 441
 Plez B., 1998, A new TiO line list, <http://sumner.berkeley.edu/>
 Plez B., Eck S. V., Jorissen A., Edvardsson B., Eriksson K., Gustafsson B., 2003, A MARCS grid of S-type Star Atmospheres
 Polyansky O. L., Kyuberis A. A., Lodi L., Tennyson J., Yurchenko S. N., Ovsyannikov R. I., Zobov N. F., 2017, *Monthly Notices of the Royal Astronomical Society*, 466, 1363
 Richardson R. S., 1931, Publications of the Astronomical Society of the Pacific, 43, 76
 Simard B., Mitchell S., Humphries M., Hackett P., 1988, *Journal of Molecular Spectroscopy*, 129, 186
 Sorensen J. J., Bernath P. F., 2021, *The Astrophysical Journal*, 923, 234
 Syme A.-M., McKemmish L. K., 2021, *Monthly Notices of the Royal Astronomical Society*, 505, 4383
 Taberner H. M., et al., 2021, *Astronomy and Astrophysics*, 646
 Tabet J., Adem Z., Taher F., 2019, *Computational and Theoretical Chemistry*, 1160, 31
 Tennyson J., Yurchenko S. N., 2012, *Monthly Notices of the Royal Astronomical Society*, 425, 21
 Tennyson J., Lodi L., McKemmish L. K., Yurchenko S. N., 2016, *Journal of Physics B: Atomic, Molecular and Optical Physics*, 49, 102001
 Van Eck S., et al., 2017, *Astronomy and Astrophysics*, 601
 Werner H. J., et al., 2020, *Journal of Chemical Physics*, 152
 Yurchenko S. N., Lodi L., Tennyson J., Stolyarov A. V., 2016, *Computer Physics Communications*, 202, 262
 Yurchenko S. N., Al-Refaie A. F., Tennyson J., 2018, *Astronomy & Astrophysics*, 614, A131